Supplemental Material for

Loss Difference Induced Localization in a Non-Hermitian Honeycomb Photonic Lattice

Yuan Feng[1,*], Zhenzhi Liu[1,*], Fu Liu[1,†], Jiawei Yu[1], Shun Liang[1], Feng Li[1], Yanpeng Zhang[1],
Min Xiao[2,3] and Zhaoyang Zhang[1,‡]

[1]Key Laboratory for Physical Electronics and Devices of the Ministry of Education & Shaanxi Key Lab of Information Photonic Technique, School of Electronic Science and Engineering, Faculty of Electronic and Information Engineering, Xi'an Jiaotong University, Xi'an, 710049, China
[2]Department of Physics, University of Arkansas, Fayetteville, Arkansas, 72701, USA
[3]National Laboratory of Solid State Microstructures and School of Physics, Nanjing University, Nanjing 210093, China

This PDF file includes:

I. Experimental settings and energy distributions in $\boldsymbol{k}$ space

II. Susceptibility distribution calculated by the density matrix method

III. Imaginary part of the band structure and its filtering effect

IV. Comparison of wave dynamics for different excitations in $\boldsymbol{k}$ space

V. Results of energy exchanges from simulation and tight-binding model

References

*[*]Y. F. and Z. L. contributed equally to this work.
[†]fu.liu@xjtu.edu.cn
[‡]zhyzhang@xjtu.edu.cn

I. Experimental settings and energy distributions in k space

A. Experimental settings

The hexagonal coupling field (wavelength≈795 nm, frequency ω_2, vertical polarization) is established by interfering three coupling beams E_2, E_2', and E_2'' from the same external-cavity diode laser (ECDL). The angle between any two coupling beams is $2\theta \approx 0.4°$, as shown in Fig. S1. The probe field E_1 (wavelength≈795 nm, frequency ω_1, horizontal polarization) comes from the second ECDL. The probe beam has the same diameter of ~1 mm as the coupling beams. The Rb vapor cell is 5 cm in length and is heated to 120 ℃. The 1D periodic pump field (wavelength≈780.2 nm, frequency ω_3, vertical polarization) is formed by interfering two pump beams E_3 and E_3' from the third ECDL. The frequency difference between the probe and coupling fields is $\omega_1 - \omega_2 \approx 2\pi \times 3.03$ GHz. The EIT-based honeycomb photonic lattice is fromed by applying the optically-induced method for engineering periodic photonic structures in solid materials into atomic gases. Based on this configuration, we can easily calculate the lattice constant of the formed honeycomb lattice. Then, the required tangential wavevector and the incident angle for exciting the K valley can be obtained, and the incident angle is about $\varphi \approx 0.23°$. The detailed beam arrangement is schematically shown in Fig. S1.
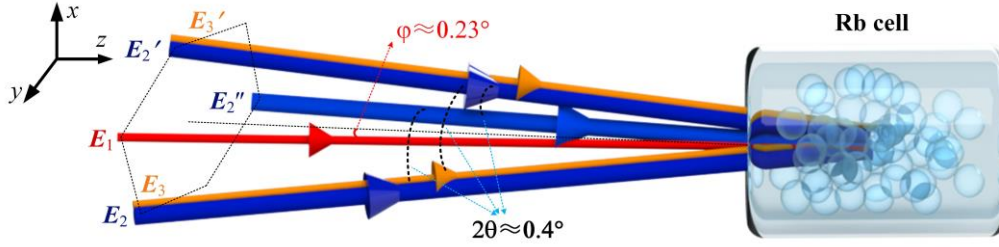

Fig. S1. The spatial beam arrangement of the system. E_2, E_2' and E_2'' (blue rays) are three coupling beams for "writing" the honeycomb photonic lattice, and the angle between each two of them is $2\theta \approx 0.4°$. Probe beam E_1 (red ray) is sent into the atomic sample to excite the vicinity of one K point with angle $\varphi \approx 0.23°$. E_3 and E_3' (orange rays) are two pump beams to establish a 1D standing-wave field to modulate the loss of the covered sublattice.

B. Energy distributions in k space

In theory, when one K valley is excited, the other two K valleys will also be excited due to the Bragg reflection during the propagation of the probe beam inside the lattice. This can be observed from the energy distribution of the beam in the reciprocal space at different propagation distance, by taking Fourier transform of the field snaps, as shown in Fig. S2(a, b). One can see that, at the initial position, the incident beam excites the vicinity of one K valley [Fig. S2(a)], while after propagating a certain distance, the other two K valleys are also excited [Fig. S2(b)], which is verified experimentally [Fig. S2(c)].
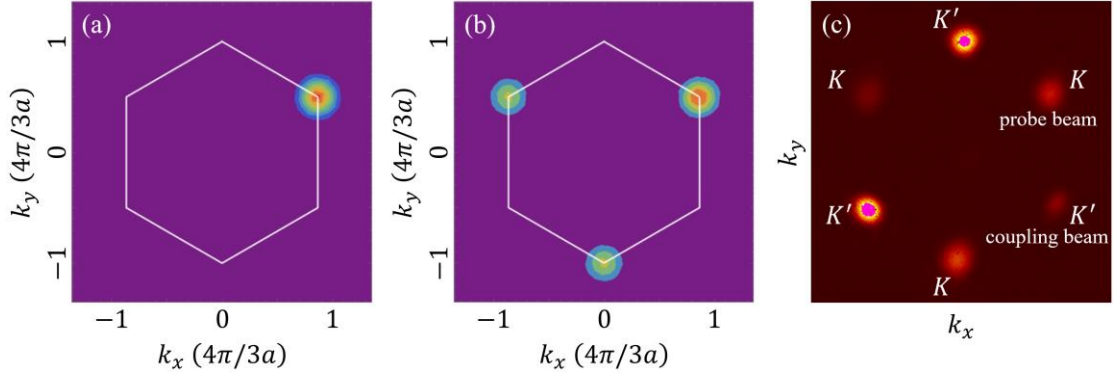
Fig. S2. (a, b) Fourier transform of the simulated Gaussian beam at initial position (a), and after it travelling through the honeycomb lattice for some distance (b). (c) The experimentally measured energy distribution of the probe beam (at K points) and the coupling beams (at three K' points) in $\boldsymbol{k}$ space after they passing through the lattice. The beam at the top right corner marked by K is the incident probe beam. The three beams marked by K' are coupling beams, which are intentionally leaked into the CCD camera to denote the positions of K' points.

II. Susceptibility distribution calculated by the density matrix method

The susceptibility distribution of the four-level N-type ^{85}Rb atomic vapor system can be approximately obtained by numerically solving the density matrix of the system [1]:

$$\dot{\rho}_{22} = \Gamma_{42}\rho_{44} + \Gamma_{32}\rho_{33} - \Gamma_{21}\rho_{22} + \frac{i}{2}(\rho_{32} - \rho_{23})\Omega_2,$$

$$\dot{\rho}_{33} = \Gamma_{43}\rho_{44} - \Gamma_{32}\rho_{33} - \Gamma_{31}\rho_{33} + \frac{i}{2}[(\rho_{23} - \rho_{32})\Omega_2 + (\rho_{13} - \rho_{31})\Omega_1],$$

$$\dot{\rho}_{44} = -(\Gamma_{43} + \Gamma_{42} + \Gamma_{41})\rho_{44} + \frac{i}{2}(\rho_{14} - \rho_{41})\Omega_3,$$

$$\dot{\rho}_{21} = -\tilde{\gamma}_{21}\rho_{21} + \frac{i}{2}(\rho_{31}\Omega_2 - \rho_{24}\Omega_3 - \rho_{23}\Omega_1),$$

$$\dot{\rho}_{31} = -\tilde{\gamma}_{31}\rho_{31} + \frac{i}{2}[\rho_{21}\Omega_2 - \rho_{34}\Omega_3 + (\rho_{11} - \rho_{33})\Omega_1],$$

$$\dot{\rho}_{41} = -\tilde{\gamma}_{41}\rho_{41} + \frac{i}{2}[-\rho_{43}\Omega_1 + (\rho_{11} - \rho_{44})\Omega_3],$$

$$\dot{\rho}_{32} = -\tilde{\gamma}_{32}\rho_{32} + \frac{i}{2}[\rho_{12}\Omega_1 + (\rho_{22} - \rho_{33})\Omega_2],$$

$$\dot{\rho}_{42} = -\tilde{\gamma}_{42}\rho_{42} + \frac{i}{2}(\rho_{12}\Omega_3 - \rho_{43}\Omega_2),$$

$$\dot{\rho}_{43} = -\tilde{\gamma}_{43}\rho_{43} + \frac{i}{2}(\rho_{13}\Omega_3 - \rho_{42}\Omega_2 - \rho_{41}\Omega_1),$$

$$\rho_{11} + \rho_{22} + \rho_{33} + \rho_{44} = 1.$$

(S1)

where ρ_{mn} are the density-matrix elements, Γ_{mn} is the natural decay rate between $|m\rangle$ level and $|n\rangle$ level. Terms $\Omega_1 = \mu_{13}E_1/\hbar$, $\Omega_2 = \mu_{23}E_2/\hbar$, and $\Omega_3 = \mu_{14}E_3/\hbar$ are the Rabi frequencies of the probe, coupling, and pump fields, respectively, with E_i being the corresponding electric-field intensity. μ_{mn} is moment of dipole for the transition $|m\rangle \rightarrow |n\rangle$. Other parameters are defined as: $\tilde{\gamma}_{21} = \gamma_{21} - i(\Delta_1 - \Delta_2)$, $\tilde{\gamma}_{31} = \gamma_{31} - i\Delta_1$, $\tilde{\gamma}_{32} = \gamma_{32} - i\Delta_2$, $\tilde{\gamma}_{41} = \gamma_{41} - i\Delta_3$, $\tilde{\gamma}_{42} = \gamma_{42} - i(\Delta_2 + \Delta_3 - \Delta_1)$, $\tilde{\gamma}_{43} = \gamma_{43} - i(\Delta_3 - \Delta_1)$ with $\gamma_{mn} = (\Gamma_n + \Gamma_m)/2$ and Δ_i (i=1, 2, 3) being the frequency detuning.

The induced susceptibility of the four-level N-type ^{85}Rb atomic vapor system can then be expressed as

$$\chi = \text{Re}(\chi) + i\text{Im}(\chi) = \frac{2N\mu_{13}\rho_{31}}{\epsilon_0 E_1} \tag{S2}$$

with N being the atomic density. For one set of the parameters: $\Omega_1 = 0.259\pi$ MHz, $\Omega_2 = 120$ MHz, $\Omega_3 = 2.5\pi$ MHz, $\Delta_1 = -50$ MHz, $\Delta_2 = -80$ MHz, and $\Delta_3 = 60$ MHz, the calculated distribution of the susceptibility χ (both real and imaginary parts) from Eq. (S2) is plotted in Fig. S3. Clearly there is loss difference between the A and B sites.
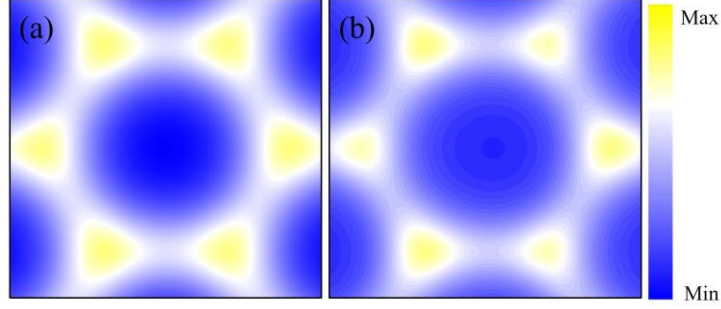

Fig. S3. Distribution of the real (a) and imaginary (b) parts of susceptibility in the multi-level atomic configuration calculated by the density matrix method.

III. Imaginary part of the band structure and its filtering effect

A. Imaginary part of the band structure

The band structures, eigenstates and propagation characteristics of the non-Hermitian honeycomb photonic lattice are obtained by solving the paraxial Schrodinger-like equation [2]:

$$i\frac{\partial \Psi}{\partial z} = -\frac{1}{2k_0}\left(\frac{\partial^2}{\partial x^2} + \frac{\partial^2}{\partial y^2}\right)\Psi - \frac{k_0\chi(x,y)}{2}\Psi \tag{S3}$$

with COMSOL Multiphysics (same for all the simulations in this work), where $\chi(x,y)$ is the susceptibility profile of the formed photonic honeycomb lattice, Ψ is the electric-field envelope. The real and imaginary parts of the band structures obtained under several different loss differences are shown in Fig. 3 (in the manuscript) and Fig. S4, respectively.
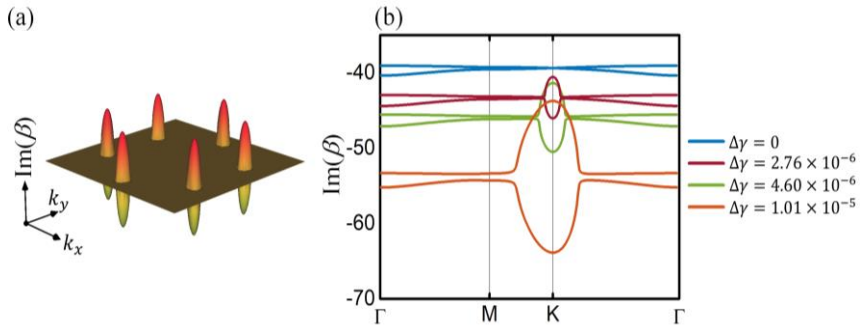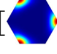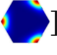

Fig. S4. (a) The imaginary part of the eigenvalues according to Eq. (2) for $\Delta\gamma = 8.5$. (b) The calculated imaginary part of band structure according to Eq. (2) for different loss difference $\Delta\gamma$.

B. Filtering effect of the imaginary part of band structure

The imaginary part of the eigenvalues $\text{Im}[\beta]$ is dispersive for large loss difference and this dispersive property of $\text{Im}[\beta]$ will introduce a filtering effect on the **k**-components of the field, thus resulting in a small variation of the field. This variation can be demonstrated by comparing the field profiles of two cases: non-dispersive and dispersive $\text{Im}[\beta]$. In our work, when there is a local flat band of $\text{Re}[\beta]$ with the presence of loss difference, there are two shared eigenstates on the local flat bands [Fig. 3(e) in the manuscript for details]:

- ψ_A [⬡]: **high-loss mode** with fields concentrated at sublattice A,

- ψ_B [⬡]: **low-loss mode** with fields concentrated at sublattice B.

With the oblique excitation of a Gaussian beam, both modes are excited. However, when the loss difference is large, ψ_A decays much quicker due to the higher loss and only the low-loss mode ψ_B survives. Therefore, for simplicity, we discuss the filtering effect considering only ψ_B, that is, with the field localized at sublattice B. In this case, the total field pattern $\Psi(x, y, z)$ is the superposition of all the **k**-components:

$$\Psi(x, y, z) = \iint_\Omega \alpha \psi_B e^{-i(k_x x + k_y y + \beta z)} \, dk_x dk_y, \tag{S4}$$

where the integration is over the whole Brillouin Zone Ω, complex β is the wavenumber along z, and α is the amplitude of the field component at (k_x, k_y) point. Now, assuming that all the contributing **k**-components fall into the local flat band (relatively large local flat band due to large loss difference), the total field pattern can be simplified as

$$\Psi(x, y, z) = \psi_B e^{-i\text{Re}[\beta]z} \iint_\Omega \alpha e^{-i(k_x x + k_y y)} e^{\text{Im}[\beta]z} dk_x dk_y, \tag{S5}$$

considering the fact that they share the same eigenvalue of $\text{Re}[\beta]$ and the same eigenstate ψ_B. From this equation one can clearly see the filtering effect of the dispersive $\text{Im}[\beta]$:

- When $\text{Im}[\beta]$ is non-dispersive, i.e., $\text{Im}[\beta]$ is a constant, the term $e^{\text{Im}[\beta]z}$ can be brought out and the integration is independent of z, indicating that the total field pattern only subjects to a phase change besides the exponential decay along z (keep in mind that $\text{Im}[\beta]$ is negative for loss). The distribution of the field amplitude is unchanged along z.

- However, when $\text{Im}[\beta]$ is dispersive, i.e., a function of (k_x, k_y), such as following the shape of Fig. S4(a), the integration is a function of z thus the distribution of the total field amplitude is varying along z.

Furthermore, we would like to note that the filtering effect of the dispersive $\text{Im}[\beta]$ is not prominent: it certainly makes the eigenstates decay in a different rate for different **k** components. However, considering the fact that all the eigenstates are the same, the total field pattern should NOT have an obvious distortion. This is also reflected by the field snaps in Fig. S5(c).

IV. Comparison of wave dynamics for different excitations in k space

Due to the existence of loss difference, local flat bands appear near the K and K' points, but in general the bands at other positions are still dispersive. In other words, the field localization at sublattice B happens only when the wave vector of the incident beam falls inside the exceptional ring, i.e., the local flat band region is excited. This can be validated by the simulated wave dynamics of the incident beam with its wave vector falling inside or outside the exceptional ring. As shown in Fig. S5, we compare the two cases. Fig. S5(c, d) shows the field snaps at different z-positions for two kinds of excitation: (c) excitation at K point inside the local flat band, (d) excitation at P point (mid-point of Γ and K) outside the local flat band, as schematically shown in Fig. S5(a, b). It is clear that when K point is excited, there is field localization at the sublattice B (corresponding to the results in main text). While when P point is excited, i.e., the excitation is outside the local flat band, there is power exchange between sublattices A and B, as seen in Fig. S5(d), especially (d3) and (d4).
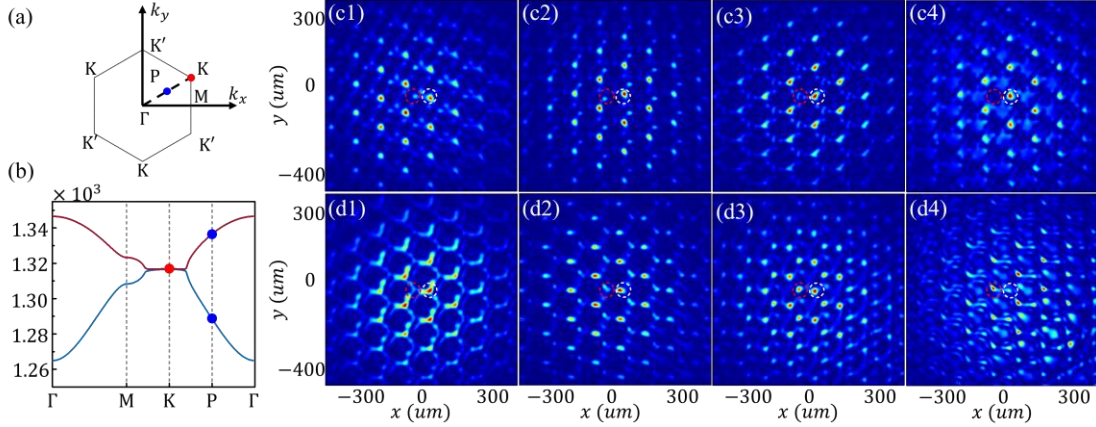

Fig. S5. (a) The excited K and P points in the first Brillouin zone. (b) The band structure of the lattice and the corresponding K and P points. The K (P) point lies inside (outside) the local flat band surface. (c, d) The field snaps at different z-positions for (c) K point and (d) P point excitation by increasing the propagation distance.

In addition, we have also performed the experiments by changing the incident angle of the probe beam. As shown in Fig. S6, one can clearly see the localization and power exchange when the probe beam is sent to excite the K point and P point, respectively.
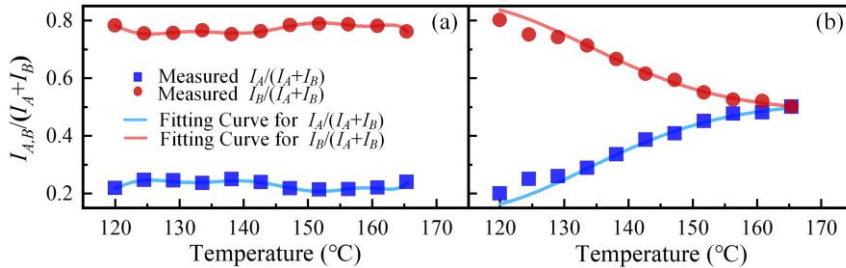

Fig. S6. Observed energy ratios of sublattices A and B during the propagation of probe beam when it is sent to K (a) and P (b) points in k space.

V. Results of energy exchanges from simulation and tight-binding model

A. Simulation results

We simulate the field localization and energy exchange behaviors of an obliquely incident Gaussian beam (probe beam) inside the synthetic honeycomb lattice with various loss differences between sublattices A and B. The Gaussian probe beam excites one K point of the lattice, and evolves in the lattice for a certain distance so that it can fully interact with the honeycomb susceptibility distribution. As plotted in Fig. S7, both the energy exchange and field localization behaviors are achieved for different $\Delta\gamma$ values. The intensities I_A and I_B are obtained by integrating the powers at the neighborhood of A and B sites, respectively. It is clear that with the increase of loss difference $\Delta\gamma$, the frequency of energy exchange gradually decreases, and the energy proportion of A (B) site gradually decreases (increases). The overall tendency of energy evolutions in simulation well supports the experimental results. The differences between the observations (Fig. 4 in the manuscript) and the simulations occur in some points, which may be caused by the existing residual Doppler effect in experiment while the theoretical model is performed under the Doppler-free condition.
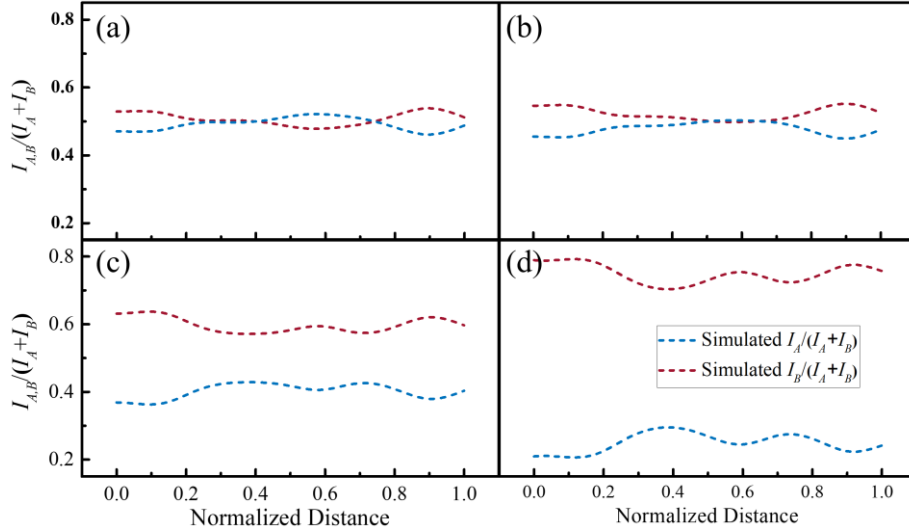

Fig. S7. Simulated energy exchanges between sublattices A and B under various loss-difference conditions with $\Delta\gamma =$ (a) 0, (b) 0.18, (c) 2.76, and (d) 9.21 ($\times 10^{-6}$), respectively.

B. Results from tight-binding model

We also calculate the propagation behaviors of the probe beam in different loss-difference scenarios by using the tight-binding model. Tight-binding model is quite accurate for describing the honeycomb lattice [3], in fact, also for modeling other lattices such as the one-dimensional SSH lattice [4], two-dimensional Lieb [5] and Kagome lattices [6], etc. While it does have simplifications on ignoring the fine structures inside each lattice site, it grabs the essential properties of the whole lattice, i.e., the average refractive index together with the representative loss/gain of each site and the coupling between neighboring sites.

The wave dynamics in the non-Hermitian honeycomb lattice with the tight-binding model is

7

described as:

$$i\partial_z A_{m,n} = -i\gamma_A A_{m,n} + \kappa\big(B_{m-1,n} + B_{m,n+1} + B_{m,n-1}\big),$$

$$i\partial_z B_{m,n} = -i\gamma_B B_{m,n} + \kappa\big(A_{m+1,n} + A_{m,n+1} + A_{m,n-1}\big),$$

(S6)

where z is the coordinate along the propagation, A and B are the fields at sites (of different sublattices) indicated by the subscripts m and n, as shown in the schematic diagram of the honeycomb lattice in Fig. S8(a), γ_A (γ_B) is the loss of A (B) sublattice, and κ is the coupling between adjacent lattice channels. With proper incident angle of the oblique Gaussian beam, the calculated energy exchanges between A and B sublattices using this tight-binding model are shown in Fig. S8(b, c), for without and with loss-difference, respectively. It is clear that the main conclusions on the energy exchange agree well with the results in Fig. 4 and Fig. S7.
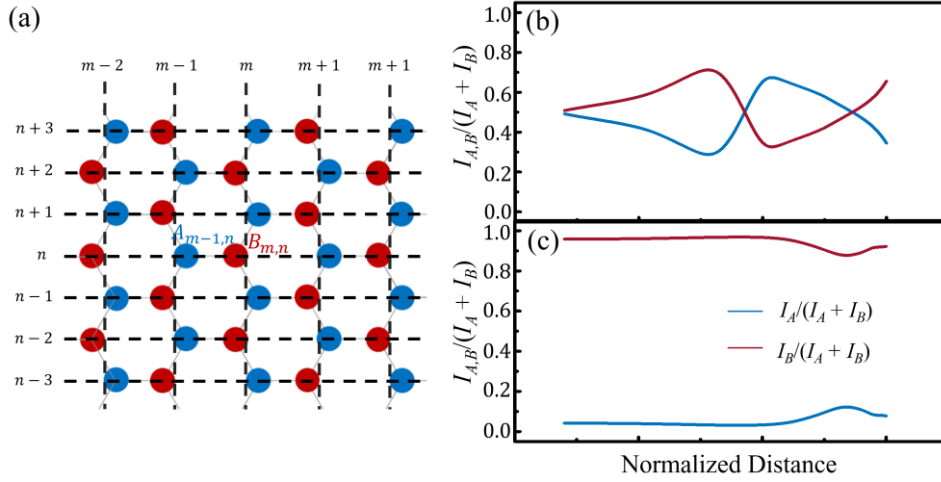

Fig. S8. (a) The schematic of the honeycomb lattice for tight-binding model, with indices defined. (b) Energy exchanges without the presence of loss difference. (c) No energy exchange with a larger loss difference.

References

[1] H. Kang, L. Wen, and Y. Zhu, Normal or anomalous dispersion and gain in a resonant coherent medium, *Phys. Rev. A* **68**, 063806 (2003).

[2] Z. Zhang, S. Ning *et al.*, Experimental demonstration of optical Bloch oscillation in electromagnetically induced photonic lattices, *Fundam. Res.* **2**, 401 (2022).

[3] M. Kremer, T. Biesenthal *et al.*, Demonstration of a two-dimensional PT-symmetric crystal, *Nat. Commun.* **10**, 435 (2019).

[4] G. Cáceres-Aravena, B. Real *et al.*, Experimental observation of edge states in SSH-Stub photonic lattices, *Phys. Rev. Res.* **4**, 013185 (2022).

[5] D. Leykam, O. Bahat-Treidel, and A. S. Desyatnikov, Pseudospin and nonlinear conical diffraction in Lieb lattices, Phys. R*ev. A* **86**, 031805(R) (2012).

[6] J. Ma, J.-W. Rhim *et. al.*, Direct Observation of Flatband Loop States Arising from Nontrivial Real-Space Topology, *Phys. Rev. Lett.* **124**, 183901 (2020).